Liu *et al. Energy Mater.* **2025**, *5*, 500144
DOI: 10.20517/energymater.2025.97

Energy Materials

Article

Open Access

Enhancing the activity and stability of RuO_2-based catalyst *via* nano-confinement effect for O_2 evolution reaction in acid electrolyte

Shukai Liu[1,2], Huang Tan[3], Gaole Dai[2], Shiyun Xiong[3], Yu Zhao[2], Benxia Li[1]

[1]School of Chemistry and Chemical Engineering, Key Laboratory of Surface & Interface Science of Polymer Materials of Zhejiang Province, Zhejiang Sci-Tech University, Hangzhou 310018, Zhejiang, China.
[2]College of Materials, Chemistry and Chemical Engineering, Key Laboratory of Organosilicon Chemistry and Material Technology (Ministry of Education), Hangzhou Normal University, Hangzhou 311121, Zhejiang, China.
[3]School of Materials and Energy, Guangzhou Key Laboratory of Low-Dimensional Materials and Energy Storage Devices, Guangdong University of Technology, Guangzhou 510006, Guangdong, China.

***Correspondence to:** Prof. Benxia Li, School of Chemistry and Chemical Engineering, Key Laboratory of Surface & Interface Science of Polymer Materials of Zhejiang Province, Zhejiang Sci-Tech University, 928 Second Avenue, Hangzhou 310018, Zhejiang, China. E-mail: libx@zstu.edu.cn; Prof. Yu Zhao, College of Materials, Chemistry and Chemical Engineering, Key Laboratory of Organosilicon Chemistry and Material Technology (Ministry of Education), Hangzhou Normal University, 2318 Yuhangtang Rd., Hangzhou 311121, Zhejiang, China. E-mail: yuzhao@hznu.edu.cn

How to cite this article: Liu, S.; Tan, H.; Dai, G.; Xiong, S.; Zhao, Y.; Li, B. Enhancing the activity and stability of RuO_2-based catalyst *via* nano-confinement effect for O_2 evolution reaction in acid electrolyte. *Energy Mater.* **2025**, *5*, 500144. https://dx.doi.org/10.20517/energymater.2025.97

Received: 10 Jun 2025 **First Decision:** 27 Jun 2025 **Revised:** 17 Jul 2025 **Accepted:** 29 Jul 2025 **Published:** 2 Sep 2025

Academic Editor: Ho Won Jang **Copy Editor:** Fangling Lan **Production Editor:** Fangling Lan

Abstract

The oxygen evolution reaction (OER), as a pivotal process in electrochemical water splitting, directly determines energy conversion efficiency. Ruthenium (Ru)-based catalysts have gained considerable attention in recent years due to their decent intrinsic activity in acidic media. Previous studies have demonstrated that while Ru exhibits superior OER activity compared to RuO_2 in acidic environments, its operational stability remains markedly inferior. This performance dichotomy, coupled with the persistent challenges of active species dissolution and catalyst particle aggregation during prolonged operation, significantly hinders their practical implementation in electrochemical systems. To address these challenges, this study develops a carbon nanotube (CNT)/Fe-Ni@RuO_2@PANI-350 composite catalyst composed of RuO_2 nanoparticles supported on bimetallic Fe-Ni modified CNTs (CNT/Fe-Ni) and encapsulated with polyaniline (PANI). This catalyst utilizes the anchoring effect of bimetallic Fe-Ni sites and the spatial confinement effect of PANI coating layer, effectively inhibiting the dissolution and agglomeration of RuO_2 during both high-temperature processing and electrochemical operation, thereby

significantly enhancing electrochemical stability. The anchoring strength of RuO_2 nanoparticles on CNT/Fe-Ni support *via* the nano-confinement effect, as well as the microscopic mechanisms underlying the performance enhancement, are revealed by density functional theory calculations and experimental characterizations. The composite catalyst demonstrates fascinating OER performance in 0.5 M H_2SO_4, exhibiting a low Tafel slope of 39.1 mV dec^{-1} as well as low overpotentials of 188 and 225 mV at current densities of 10 and 100 mA cm^{-2}, respectively. Remarkably, the composite catalyst demonstrates significantly enhanced stability, exhibiting only ~30 mV overpotential increase during 150 h continuous operation at 10 mA cm^{-2}. This study highlights a simple yet effective nano-confinement strategy to address the challenges of Ru-based catalysts, and provides a practical paradigm for designing and preparing highly efficient OER electrocatalysts with enhanced stability.

Keywords: Oxygen evolution reaction (OER), ruthenium (Ru)-based catalysts, nano-confinement strategy, electrochemical stability

INTRODUCTION

Electrochemical water splitting is recognized as one of the most promising methods for producing H_2, which is considered perhaps the ultimate sustainable and clean energy resource in modern society[1,2]. Electrochemical water splitting comprises the hydrogen evolution reaction (HER) at the cathode and the oxygen evolution reaction (OER) at the anode. Compared to HER, OER exhibits sluggish kinetics due to its complex multi-electron and proton transfer processes, making it the rate-determining step in an overall water-electrolysis process[3-5]. The high overpotentials required for OER, particularly in acidic electrolytes, and the poor stability of electrocatalysts further hinder its practical applications[6,7]. Thus, developing high-performance OER electrocatalysts in acidic environment remains challenging. In previous studies on OER catalysts, Ruthenium (Ru)-based catalysts have attracted much attention due to their relatively high activity in acidic media[8].

However, Ru-based catalysts are facing significant challenges including high cost, particle aggregation at elevated temperature during preparation, poor electrochemical stability[9-14], particularly under strong oxidizing conditions or exposed acidic electrolytes where the dissolution of Ru species leads to active site loss and rapid performance degradation[15-17]. Among these challenges, the dissolution of Ru species is directly related to stability deterioration and lifespan shortening[18].To address this challenge, previous studies have proposed various strategies, including metal doping[19], heterostructure engineering[20], defect engineering[21], morphology control[22], and modifications of catalyst supports[23]. Generally, the selection of catalyst supports plays a critical role in determining catalytic performance, as they profoundly influence the activity, stability, and electron transfer properties[24-27]. Carbon-based materials, particularly carbon nanotubes (CNTs), have emerged as prominent candidates in catalyst support research due to their exceptional electrical conductivity, large specific surface area, and superior chemical stability[28].

In this study, Fe-Ni co-modified CNTs (CNT/Fe-Ni) were designed as the support of Ru-based catalysts, and the catalytic activity and stability of RuO_2 in OER under acidic conditions were investigated. The CNT/Fe-Ni material was synthesized via chemical vapor deposition (CVD), where ferrocene and nickelocene served not only as the catalyst for CNT growth but also as precursors to *in situ* form the Fe-Ni anchor sites for subsequent RuO_2 growth *via* nano-confinement effect. Thereafter, the nanostructure is stabilized by coating with a polyaniline (PANI) layer, to prevent the agglomeration of RuO_2 nanoparticles during the subsequent high-temperature treatment and electrochemical operation. Such a structure design of the composite catalyst leverages the anchoring effect of bimetallic Fe-Ni alloy to facilitate the confined growth of RuO_2 nanoparticles on Fe-Ni alloy sites and establish a strong metal-support interaction. This design not only utilizes the high conductivity and large specific surface area of CNTs, but also optimizes the Ru active

sites through interfacial electronic coupling between Ni, Fe, and Ru, thereby significantly enhancing the catalytic activity and stability of the catalyst during OER process. This study underscores a simple yet effective nano-confinement strategy to address challenges faced by Ru-based catalysts in acidic environments, providing a practical paradigm for designing and preparing highly efficient OER electrocatalysts with enhanced stability.

EXPERIMENTAL

Chemicals and materials

Ferrocene (high purity, ≥ 99.5%) was purchased from Alfa Aesar. Nickelocene (analytical grade, ≥ 98.0%) was obtained from Macklin. $RuCl_3$ (analytical grade, ≥ 97.0%) was supplied by Ark Pharm. Urea (analytical grade, ≥ 99.0%) and ammonium persulfate (APS, analytical grade, ≥ 98.0%) were procured from Aladdin. Acetonitrile (analytical grade, ≥ 99.5%) was purchased from Sinopharm Chemical Reagent Co., Ltd. Aniline (analytical grade, ≥ 99.0%) was obtained from Alfa Aesar, while isopropanol (analytical grade, ≥ 99.7%) was supplied by Shanghai Lingfeng Chemical Reagent Co., Ltd. Nafion solution (5%, D520, DuPont) was purchased from Shanghai Hesen Electric Co., Ltd. All chemicals used in this work were employed without further purification.

Preparation of CNT/Fe-Ni support

A total of 50 mg of nickelocene and 50 mg of ferrocene were placed at the low-temperature zone of a tubular furnace, maintaining a constant Ar flow rate of 300 sccm inside the tube. When the furnace temperature reached 850 °C (heating rate: 4 °C min^{-1}), an acetonitrile:ethanol mixture (v/v = 3:1) was heated to 90 °C, and the resulting vapor was introduced into the furnace using an Ar carrier gas. After 5 min of reaction, the product was cooled to obtain CNT/Fe-Ni.

Synthesis of CNT/Fe-Ni@RuO_2-350

A total of 45 mg of CNT/Fe-Ni was dispersed in 42 mL of ethanol, followed by the addition of 45 mL of deionized (DI) water. The mixture was ultrasonicated for 5 min. Under continuous stirring, 3 mL of 0.05 M $RuCl_3$ solution and 300 mg of urea were added. The homogeneous solution was then transferred into a 150 mL Teflon-lined autoclave and subjected to a hydrothermal reaction at 180 °C for 4 h. After cooling to room temperature, the product was thoroughly washed with water and ethanol via centrifugation and dried in an oven at 55 °C to obtain CNT/Fe-Ni@RuO_2. The dried sample was calcined in a muffle furnace at 350 °C for 4 h (heating rate: 2 °C min^{-1}) to yield the final CNT/Fe-Ni@RuO_2-350 material.

The control samples, CNT/Ni@RuO_2-350 and CNT/Fe@RuO_2-350, were synthesized using 0.1 g of nickelocene and ferrocene, respectively, as catalysts for the preparation of CNT/Ni and CNT/Fe, while the subsequent steps remained unchanged.

Synthesis of CNT/Fe-Ni@RuO_2@PANI-350

A total of 40 mg of CNT/Fe-Ni@RuO_2 was dispersed in 40 mL of DI water via ultrasonication. The resulting mixture was placed in an ice bath, followed by the addition of 10 mL of 0.5 M HCl containing 60 μL of aniline and another 10 mL of 0.5 M HCl containing 120 mg of APS. The reaction system was continuously stirred in an ice bath for 10 h. The obtained product was washed thoroughly with water and ethanol via centrifugation and subsequently dried in an oven at 55 °C. The dried sample was then calcined in a muffle furnace at 350 °C for 4 h (heating rate: 2 °C min^{-1}) to obtain CNT/Fe-Ni@RuO_2@PANI-350.

The control samples, CNT/Ni@RuO_2@PANI-350 and CNT/Fe@RuO_2@PANI-350, were synthesized using 0.1 g of nickelocene and ferrocene, respectively, as catalysts for the preparation of CNT/Ni and CNT/Fe, while the subsequent steps remained unchanged.

Characterization

Powder X-ray diffraction (XRD) patterns were recorded using a Bruker D8 Advance Davinci diffractometer (Germany) with Cu Kα radiation (λ = 1.54178 Å). Surface morphology and elemental composition were analyzed using a field emission scanning electron microscope (SEM, Zeiss Supra55, GER) and a high-resolution transmission electron microscope (HR-TEM, JEM-2100, JEOL, Japan), with corresponding energy-dispersive X-ray spectroscopy (EDS) data collected. X-ray photoelectron spectroscopy (XPS) analysis was performed on an ESCALAB 250Xi spectrometer (Thermo Fisher, USA) with monochromatic Al Kα radiation (150 W), calibrated to the C 1s peak at 284.8 eV. Raman spectra were carried out on a Spelec Raman spectrometer with 532 nm laser.

Electrochemical measurements

Electrochemical measurements were conducted using a CHI 760E electrochemical workstation (Shanghai Chenhua Instrument Co., Ltd.). A conventional three-electrode system was employed, with a 3 mm-diameter glassy carbon electrode (GC) as the working electrode, a carbon rod as the counter electrode, and an Ag/AgCl electrode as the reference electrode. The catalyst ink was drop-cast onto the GC electrode and dried under an infrared lamp to prepare the working electrode. Catalyst ink was prepared by dispersing 5.0 mg of catalyst in a 1.0 mL water/isopropanol (3:1, v/v) mixture containing 10.0 μL of 5.0% Nafion solution (Sigma-Aldrich), followed by ultrasonication for 30 min. Prior to catalyst loading, the GC electrode was sequentially polished using 0.1 and 0.03 μm Al_2O_3 powder and rinsed with DI water. The catalyst loading was controlled at ~0.35 mg cm^{-2}.

The linear sweep voltammetry (LSV) measurements were conducted at a scan rate of 5.0 mV s^{-1} in an electrolyte of 0.5 M H_2SO_4. The potentials measured in the three-electrode system were converted to the corresponding reversible hydrogen electrode (RHE) potentials using the transformation equation: $E_{RHE} = E_{Ag/AgCl} + 0.0592 \times pH + 0.197$. Unless otherwise specified, all data were corrected for 90% IR compensation. The time-potential curve was recorded by maintaining the current density of the working electrode at 10.0 mA cm^{-2}. Prior to LSV testing, the catalyst was activated via 20 cycles of cyclic voltammetry (CV) testing.

The electrochemical impedance spectroscopy (EIS) measurements were performed at 1,600 rpm under an applied potential of 1.45 V *vs.* RHE, within a frequency range of 10^5-10^{-1} Hz. The electrochemical double-layer capacitance (C_{dl}) of the catalyst was estimated by measuring at different scan frequencies within the potential range of 1.1-1.2 V *vs.* RHE. The C_{dl} value was determined from the slope of the linear relationship between the half-difference of the anodic and cathodic current densities ($\Delta j = j_{anode} - j_{cathode}$) and the scan rate (ν) at 1.15 V *vs.* RHE. The electrochemically active surface area (ECSA) of the catalyst was calculated using $ECSA = C_{dl} \cdot S/C_s$, where C_s is the roughness factor with a value of 35 μF cm^{-2}, and S is the geometric area of the electrode. For long-term time-potential measurements, a carbon paper electrode loaded with the catalyst (mass loading 1.5 mg cm^{-2}) was used as the working electrode, with the current density maintained at 10.0 mA cm^{-2}.

DFT

The spin-polarized density functional theory (DFT) calculations were performed using the Vienna Ab initio Simulation Package (VASP)[29-31]. The projector augmented-wave (PAW) method was employed to describe the core-valence electron interactions[32]. The exchange-correlation interactions were treated within the generalized gradient approximation (GGA) using the Perdew-Burke-Ernzerhof (PBE) functional[33]. Structural optimizations and static self-consistent calculations were conducted with Gamma-centered 1 × 1 × 1 and 3 × 3 × 1 k-point meshes, respectively. A plane-wave cutoff energy of 450 eV was adopted. The energy convergence threshold was set to 1×10^{-6} eV, while the force convergence criterion was 0.02 eV/Å. A

vacuum layer of 20 Å was introduced to minimize periodic interactions between adjacent slabs. Long-range van der Waals interactions were accounted for using the DFT-D3 dispersion correction method[34].

The OER activity of the catalyst was evaluated through the computational hydrogen electrode (CHE) model proposed by Nørskov *et al.*[35]. This model considers four elementary steps, with the Gibbs free energy change for each step calculated using [which incorporates zero-point energy (ZPE) correction and entropy contribution (TS)]:

$$\Delta G = \Delta E + \Delta ZPE - T\Delta S + \Delta G_U \quad (1)$$

Here, ΔE represents the binding energy change of intermediate species (e.g., *OH, *O, *OOH), and $\Delta G_U = -eU$ (where U denotes the applied electrode potential). Differential charge density analysis and global average differential charge density profiles were obtained using the VASPKIT toolkit[36].

RESULTS AND DISCUSSION

The Fe-Ni modified CNTs (CNT/Fe-Ni) were synthesized via CVD using a mixed solvent of ethanol and acetonitrile with varying ratios as the carbon source under Ar carrier gas, using both nickelocene and ferrocene as the catalysts for CNT growth. Scanning electron microscopy (SEM) images of the CNT/Fe-Ni samples synthesized with varying volume ratios of ethanol to acetonitrile are shown in Supplementary Figure 1. These CNT/Fe-Ni samples consist of CNTs with varied aspect ratios. Notably, when the volume ratio of ethanol to acetonitrile is 2:3, the CNTs with a uniform diameter of ca. 150 nm (denoted as CNT/Fe-Ni) were obtained [Supplementary Figure 2]. The RuO_2-decorated CNT/Fe-Ni (denoted as CNT/Fe-Ni@RuO_2) was synthesized *via* a solvothermal reaction using CNT/Fe-Ni and $RuCl_3$ as precursors. Subsequently, a PANI layer was polymerized on the surface of CNT/Fe-Ni@RuO_2 to form CNT/Fe-Ni@RuO_2@PANI, which was further calcined in air at 350 °C for 4 h to obtain the final CNT/Fe-Ni@RuO_2@PANI-350 catalyst [Scheme 1].

The structure of CNT/Fe-Ni is first characterized by XRD and XPS. The diffraction peak of graphitic carbon [Supplementary Figure 3A] could be clearly observed, but the characteristic diffraction peak of Fe-Ni alloy was rather weak, indicating the particle size of the generated Fe-Ni alloy is either too small or highly dispersed in the carbon matrix. In the Fe 2p XPS spectrum [Supplementary Figure 4], the peaks at binding energies of 707.2, 711.2 and 713.3 eV correspond to Fe^0, Fe^{2+}, and Fe^{3+}, respectively, with a satellite peak at 717.8 eV (Fe $2p_{3/2}$). Similarly, in the Ni $2p_{3/2}$ spectrum, the peaks at binding energies of 852.6, 853.8 and 855.0 eV are related to Ni^0, Ni^{2+}, and Ni^{3+}, respectively, with a satellite peak at 861.7 eV. The existence of Fe^0 and Ni^0 demonstrated that they exist in metallic and/or alloying counterparts, consistent with XRD analysis. The high valence states of Fe (Fe^{2+}, Fe^{3+}) and Ni (Ni^{2+}, Ni^{3+}) might result from the surface oxidation of metallic Fe and Ni[13].

The morphology of CNT/Fe-Ni, CNT/Fe-Ni@RuO_2, CNT/Fe-Ni@RuO_2@PANI and CNT/Fe-Ni@RuO_2@PANI-350 is investigated by transmission electron microscopy (TEM). The representative TEM image of CNT/Fe-Ni [Figure 1A] displays the nanotube with a diameter of 150 nm. The high-resolution TEM image (insert in Figure 1A) reveals an average interplanar spacing of 0.345 nm, which is assigned to the (002) crystal plane of graphite, indicating that the CNTs exhibit high crystallinity[37]. After the hydrothermal reaction at either low or high $RuCl_3$ concentration, RuO_2 nanoparticles are observed to be anchored on the surface of CNT/Fe-Ni with high uniformity, as shown in Figure 1B, indicating that Fe-Ni on the CNT/Fe-Ni surface is likely to induce a nano-confinement effect for preferentially depositing RuO_2 nanoparticles on the Fe-Ni sites. Such an effect promotes strong metal-support interaction, which is expected to stabilize Ru

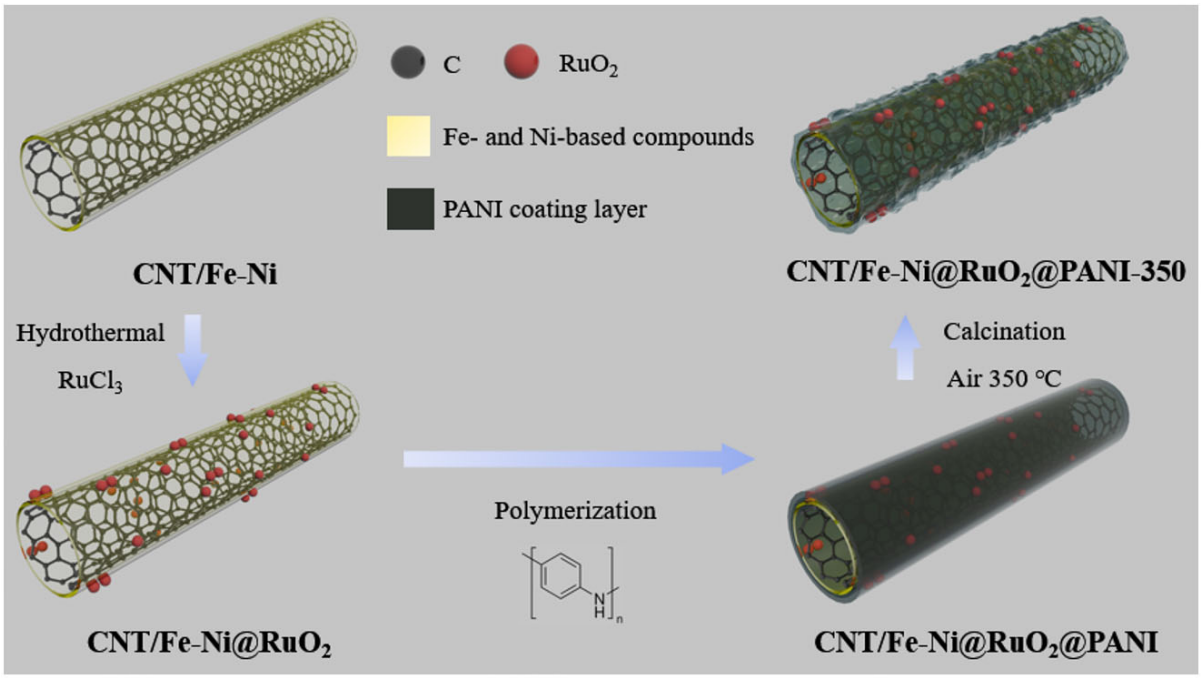

Scheme 1. Schematic illustration of the synthesis of CNT/Fe-Ni@RuO_2@PANI-350.

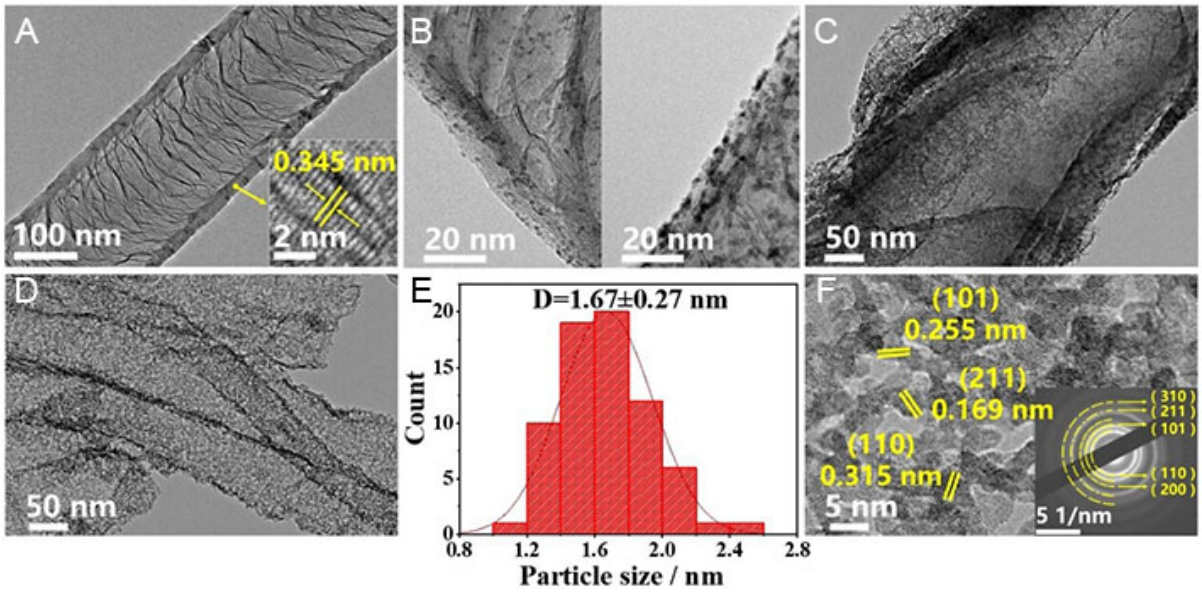

Figure 1. TEM characterization of CNT/Fe-Ni, CNT/Fe-Ni@RuO_2, CNT/Fe-Ni@RuO_2@PANI and CNT/Fe-Ni@RuO_2@PANI-350. TEM images of (A) CNT/Fe-Ni; (B) CNT/Fe-Ni@RuO_2 with low (left) and high (right) RuO_2 loading; (C) CNT/Fe-Ni@RuO_2@PANI, (D) CNT/Fe-Ni@RuO_2@PANI-350; (E) Particle size distribution histogram of CNT/Fe-Ni@RuO_2@PANI-350. (F) IFFT image of CNT/Fe-Ni@RuO_2@PANI-350, inset: corresponding SAED image.

species during the OER process. Figure 1C and D display a typical TEM image of CNT/Fe-Ni@RuO_2@PANI and CNT/Fe-Ni@RuO_2@PANI-350. The coating of PANI prevents the agglomeration of RuO_2 nanoparticles during high-temperature treatment. The TEM image of CNT/Fe-Ni@RuO_2@PANI-350 demonstrates the uniform distribution of RuO_2 nanoparticles which exhibit an average size of 1.67 ± 0.27 nm [Figure 1E]. The

high-resolution TEM image shown in Figure 1F reveals the high crystallinity of RuO_2 nanoparticles. The lattice spacing of 0.315, 0.255 and 0.169 nm corresponded to the (110), (101) and (201) crystal planes of the rutile-structured RuO_2. This observation aligns well with the selected-area electron diffraction (SAED) pattern shown in Figure 1F, which exhibits distinct diffraction rings that are assigned to the (110), (101), and (211) planes of rutile RuO_2. These findings confirm the successful formation of RuO_2 NPs anchored on the CNT/Fe-Ni framework.

Figure 2A shows the XRD pattern of the CNT/Fe-Ni@RuO_2@PANI-350 sample. The sharp peak at 26.5° is the characteristic diffraction peak of (002) crystal plane of graphitic carbon (PDF# 75-1621), and the (110), (101) and (211) crystal planes of rutile RuO_2 (PDF# 71-2273) are also observed, further confirming the crystalline nature of the CNT as well as the presence of RuO_2. XPS measurements were conducted to obtain more structural information about the CNT/Fe-Ni@RuO_2@PANI-350 catalyst. Ru, Fe, Ni, O, C, and N elements were detected as shown in the survey XPS spectrum [Figure 2B]. Supplementary Figure 5 displays the scanning transmission electron microscopy (STEM) and EDS elemental mapping images of the CNT/Fe-Ni@RuO_2@PANI-350 catalyst, demonstrating the uniform distribution of C, N, Fe, Ni throughout the CNT/Fe-Ni support as well as Ru and O from RuO_2 uniformly distributed on the CNT/Fe-Ni support. The N element was introduced from the acetonitrile precursor and PANI. The high-resolution C 1s and Ru 3d spectra are shown in Figure 2C. The peak at a binding energy of 284.8 eV corresponds to the characteristic C=C bond in graphite, and the peak at a binding energy of 285.8 eV is attributed to C-N bonds in CNT/Fe-Ni@RuO_2@PANI-350. For the Ru 3d spectrum, the peaks at 281.1 and 285.4 eV correspond to Ru $3d_{5/2}$ and Ru $3d_{3/2}$ of RuO_2 with satellite peaks observed at 282.8 and 286.2 eV for Ru $3d_{5/2}$ and Ru $3d_{3/2}$, respectively. The XPS spectra of Fe 2p and Ni 2p for CNT/Fe-Ni@RuO_2@PANI-350 [Supplementary Figure 6] are similar to those of CNT/Fe-Ni. The peaks centered at 705.5, 710.8/724.4 and 712.9/726.4 eV are assigned to Fe^0, Fe^{2+} and Fe^{3+}, respectively. The peaks centered at 850.6, 854.1 and 856.0 eV arise from Ni^0, Ni^{2+} and Ni^{3+}, respectively. The XPS analyses confirm the presence of Fe-Ni in the CNT/Fe-Ni@RuO_2@PANI-350 catalyst. Figure 2D displays the Ru $3p_{3/2}$ spectrum of CNT/Fe-Ni@RuO_2@PANI-350, featuring binding energies at 462.8 eV (Ru^{4+}) and 465.3 eV (Ru^{3+}). The presence of Ru^{3+} indicates the existence of oxygen vacancies (V_O) in RuO_2 NPs. In O 1s spectrum [Figure 2E], the peaks at binding energies of 529.7, 530.5, and 532.0 eV are associated with the lattice oxygen (O_L) in RuO_2, the oxygen in Ru-OH bond and C=O/C-O bonds, respectively. In addition, the peaks at 531.2 and 533.0 eV correspond to the oxygen adjacent to V_O and the surface-adsorbed oxygen-containing species, respectively. The formation of V_O in CNT/Fe-Ni@RuO_2@PANI-350 is attributed to the reaction between RuO_2 and carbon during the thermal treatment of CNT/Fe-Ni@RuO_2@PANI: $RuO_2 + C \rightarrow V_O\text{-}RuO_2 + CO_2$[38]. Besides, the synergistic effect between Fe-Ni and CNT can promote the formation of active sites[39]. Therefore, the integration of defective RuO_2 with CNT/Fe-Ni is expected to promote the electrochemical performance of CNT/Fe-Ni@RuO_2@PANI-350. Supplementary Figure 3B displays the Raman spectra of both CNT/Fe-Ni@RuO_2@PANI-350 and CNT/Fe-Ni samples. It reveals that the CNT/Fe-Ni sample exhibits a lower graphitization degree. Carbon-based materials with reduced graphitization may contain more structural defects, which could increase the number of edge defects and provide additional growth sites for metal species[40]. After heat treatment at 350 °C, CNT/Fe-Ni@RuO_2@PANI-350 shows a little increase in graphitization, compared with CNT/Fe-Ni. During the heat treatment at 350 °C, PANI underwent partial carbonization, and residual nitrogen species formed multiple types of active sites through doping, further enhancing the OER activity and stability of CNT/Fe-Ni@RuO_2@PANI-350 [Figures 2F and 3A]. No significant Fe/Ni-related peaks are observed in the Raman spectra, likely due to the relatively low sensitivity of Raman spectroscopy to metallic phases. Figure 2F shows the N 1s spectrum of CNT/Fe-Ni@RuO_2@PANI-350, with characteristic binding energies of pyridinic N (398.2 eV), pyrrolic N (399.8 eV), graphitic N (400.9 eV), and oxidized N (402.1 eV). The analytical results of XPS calculations presented in Supplementary Table 1 demonstrate that the relative weight percentage of RuO_2 in CNT/Fe-Ni@RuO_2@PANI-350 is 40.7 wt%.

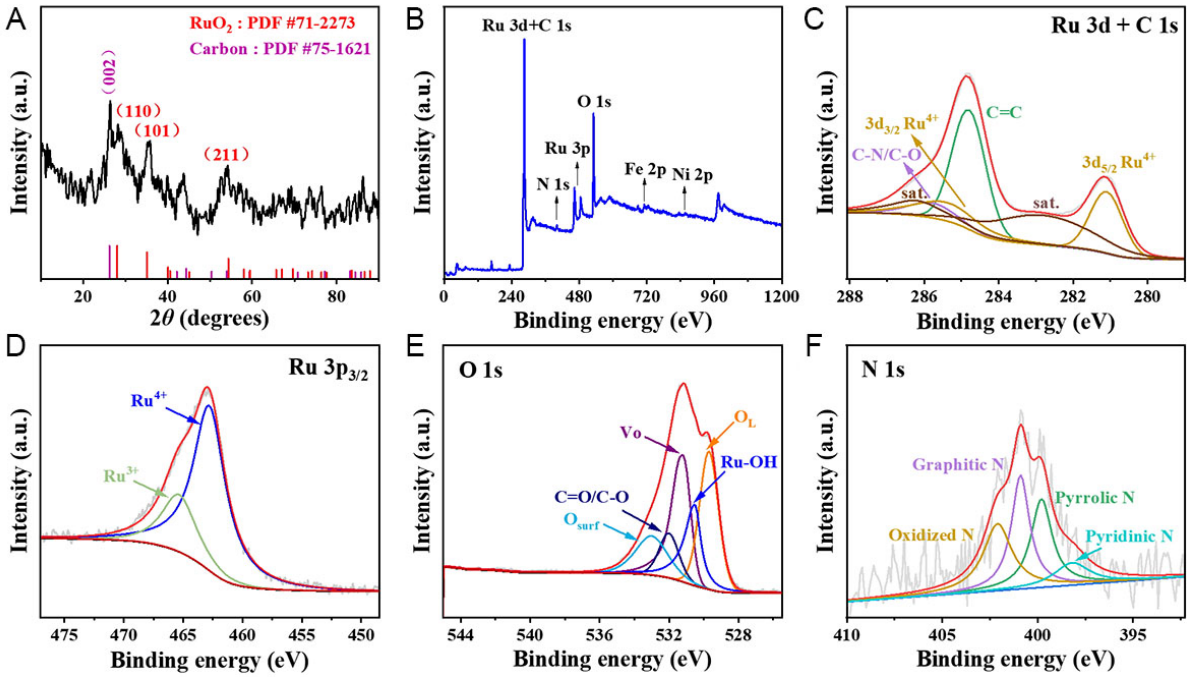

Figure 2. XRD and XPS characterization of CNT/Fe-Ni@RuO_2@PANI-350. (A) XRD pattern, (B) XPS survey spectrum, (C) Ru 3d and C 1s spectrum, (D) Ru $3p_{3/2}$ spectrum, (E) O 1s spectrum, and (F) N 1s spectrum.

Figure 3 illustrates the OER catalytic performance of CNT/Fe-Ni@RuO_2@PANI-350 in acidic conditions. Meanwhile, the OER catalytic performance of the catalyst prepared by only using ferrocene (denoted as CNT/Fe@RuO_2@PANI-350) or nickelocene (denoted as CNT/Ni@RuO_2@PANI-350) was also investigated for better comparison and to highlight the synergic effect of Fe-Ni alloy. As shown in Figure 3A, CNT/Fe-Ni@RuO_2@PANI-350 exhibits the best OER activity, with an overpotential (η_{10}) of only ca. 188 mV at a current density of 10 mA cm^{-2}. The overpotential (η_{10}) of CNT/Fe-Ni@RuO_2@PANI-350 is significantly lower than those of CNT/Fe@RuO_2@PANI-350 (234 mV), CNT/Ni@RuO_2@PANI-350 (259 mV), and the other catalysts without PANI coating. The previous study has demonstrated that the catalysts with PANI modification exhibited better performance than the ones without PANI modification[38]. As displayed in Figure 3B, the η_{10} values of CNT/Fe-Ni@RuO_2@PANI-350, CNT/Fe@RuO_2@PANI-350 and CNT/Ni@RuO_2@PANI-350 are lower than those of CNT/Fe-Ni@RuO_2-350, CNT/Fe@RuO_2-350 and CNT/Ni@RuO_2-350, respectively. This is potentially because the presence of PANI on the catalyst surface induces the formation of an ultra-thin carbon layer and abundant V_Os in RuO_2 NPs during the calcination process, resulting in the improved catalytic activity of RuO_2. The corresponding Tafel plots shown in Figure 3C indicate that CNT/Fe-Ni@RuO_2@PANI-350 possesses the smallest Tafel slope of only 39.1 mV dec^{-1}. The Fe-C hetero-interface in CNT/Fe-Ni enhances the synergistic effect between metal and CNT, promoting the formation of active sites and improving catalytic activity[41,42]. Furthermore, the catalytic activity can be further enhanced by the introduction of Ni. As indicated in Figure 3D, CNT/Fe-Ni@RuO_2@PANI-350 shows significantly improved OER catalytic activity compared with CNT/Fe@RuO_2@PANI-350. The overpotentials at the current density of 10 and 100 mA cm^{-2} are reduced from 234 and 274 mV to 188 and 225 mV, respectively. Moreover, the catalytic activity of CNT/Fe-Ni@RuO_2@PANI-350 surpasses that of commercial RuO_2/CC (η_{10} = 310 mV), and most reported catalysts such as B-RuO_2 (η_{10} = 200 mV)[43] and PtCo-RuO_2/C (η_{10} = 212 mV)[44] as summarized in Supplementary Table 2. These results verify the superior OER activity of CNT/Fe-Ni@RuO_2@PANI-350 in acidic media. At a higher current density of 100 mA cm^{-2} [Figure 3D], CNT/Fe-Ni@RuO_2@PANI-350 maintains a low overpotential (η_{100}) of 225 mV, which is significantly lower than those of

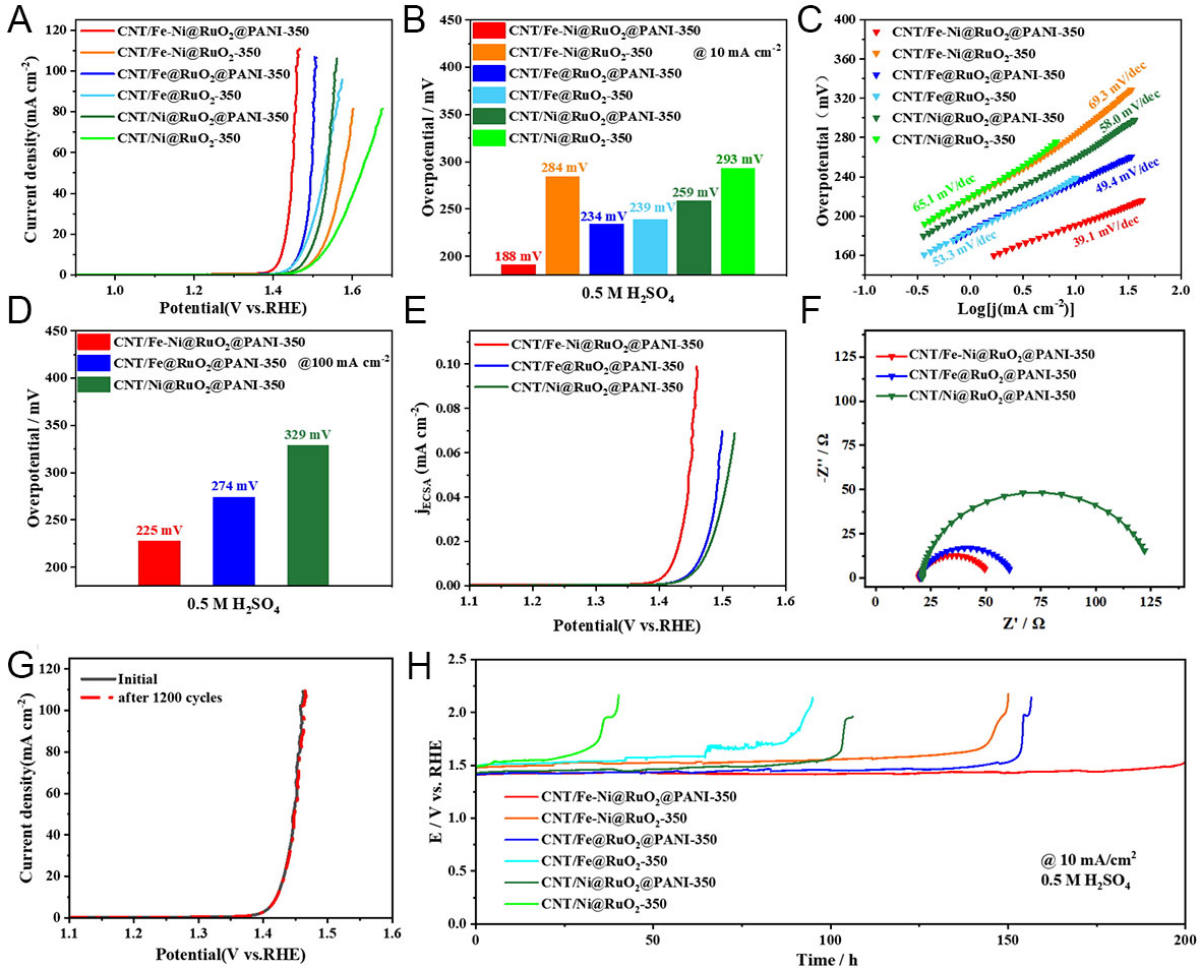

Figure 3. OER catalytic performance of different catalysts in 0.5 M H_2SO_4 solution. (A) OER polarization curves, (B) overpotentials at a current density of 10.0 mA cm^{-2}, (C) Tafel plots, (D) overpotentials at a current density of 100.0 mA cm^{-2}, (E) ECSA-normalized polarization profiles, (F) EIS spectra, (G) polarization profiles of CNT/Fe-Ni@RuO_2@PANI-350 before and after OER, (H) time-dependent potential curves.

CNT/Fe@RuO_2@PANI-350 (η_{100} = 274 mV) and CNT/Ni@RuO_2@PANI-350 (η_{100} = 329 mV). Such high-current performance is more favorable for practical applications, and the CNT/Fe-Ni@RuO_2@PANI-350 catalyst exhibits remarkable advantage at the increased current density. Supplementary Figure 7 presents the OER catalytic performance of CNT/Fe-Ni, CNT/Fe-Ni@RuO_2, and CNT/Fe-Ni@RuO_2@PANI under acidic conditions. Combined with Figure 3A, it reveals that samples without Ru loading or calcination treatment exhibit lower catalytic activity, demonstrating the necessity of both Ru loading and calcination treatment.

The intrinsic activity of CNT/Fe-Ni@RuO_2@PANI-350 towards the OER reaction is further evaluated by linear sweep voltammograms (LSVs) normalized by the ECSA. The ECSA of the catalyst can be calculated based on the C_{dl} value estimated by extrapolating the cyclic voltammograms (CVs) at different scan rates [Supplementary Figure 8]. The results show that the C_{dl} value of CNT/Fe-Ni@RuO_2@PANI-350 is 34.9 mF cm^{-2}, which is higher than those of CNT/Fe@RuO_2@PANI-350 (29.0 mF cm^{-2}) and CNT/Ni@RuO_2@PANI-350 (13.8 mF cm^{-2}). A higher C_{dl} value indicates a larger exposed area of the material in the electrolyte and more active sites, which is beneficial for improving the overall catalytic activity. The intrinsic activity evaluated by ECSA is proportional to the C_{dl} (ECSA $\propto C_{dl}$)[44]. The ECSA of CNT/Fe-Ni@RuO_2

@PANI-350 calibrated by the formula is 70.5 cm^2, higher than those of CNT/Fe@RuO_2@PANI-350 (58.6 cm^2) and CNT/Ni@RuO_2@PANI-350 (27.9 cm^2). The ECSA-normalized LSVs in Figure 3E show that the overpotential of CNT/Fe-Ni@RuO_2@PANI-350 is 190 mV to drive a current density of 0.01 mA cm^{-2}, which is lower than those of CNT/Fe@RuO_2@PANI-350 (230 mV) and CNT/Ni@RuO_2@PANI-350 (236 mV). These findings verify the higher intrinsic catalytic activity of CNT/Fe-Ni@RuO_2@PANI-350 towards OER. Moreover, CNT/Fe-Ni@RuO_2@PANI-350 demonstrates a reduced electrochemical impedance during OER, with a charge-transfer resistance of 31.8 Ω, which is notably lower than those of CNT/Fe@RuO_2@PANI-350 (42.0 Ω) and CNT/Ni@RuO_2@PANI-350 (104.5 Ω), as shown in Figure 3F and Supplementary Figure 9. The lower charge transfer resistance indicates enhanced OER kinetics and an accelerated charge transfer rate in CNT/Fe-Ni@RuO_2@PANI-350. The high electrical conductivity is potentially attributed to the Fe-C strongly coupled interface, which affords an efficient electron transfer channel to enhance electron transfer efficiency[42]. Additionally, CNT/Fe-Ni@RuO_2@PANI-350 also exhibits excellent durability for OER. As shown in Figure 3G, no noticeable decrease in activity is observed after 1,200 repeated OER cycles. The time-dependent OER test [Figure 3H] demonstrates that CNT/Fe-Ni@RuO_2@PANI-350 exhibits a minimal increase of ~30 mV in overpotential over 150 h reaction. In contrast, CNT/Ni@RuO_2-350, CNT/Fe@RuO_2-350, CNT/Ni@RuO_2@PANI-350, CNT/Fe-Ni@RuO_2-350 and CNT/Fe@RuO_2@PANI-350 lost their activities after working for 40, 94, 106, 150, and 156 h, respectively, during the OER stability test. This result demonstrates that the unique structural design of CNT/Fe-Ni@RuO_2@PANI-350 can protect RuO_2 NPs from chemical corrosion during the OER. Structural characterization in the Supplementary Figure 10 indicates that CNT/Fe-Ni@RuO_2@PANI-350 possesses excellent structural robustness. Even after undergoing 150 hours of OER testing, RuO_2 NPs are still clearly observable in the CNT/Fe-Ni@RuO_2@PANI-350 catalyst. The RuO_2 NPs exhibit no significant morphological changes in particle sizes [Supplementary Figure 11] and remain uniformly distributed on the CNT/Fe-Ni support [Supplementary Figure 12]. After the OER reaction in 0.5 M H_2SO_4 electrolyte, the CNT/Fe-Ni@RuO_2@PANI-350 catalyst exhibits no significant changes in morphological feature and element distribution [Supplementary Figure 12]. The unique structural design of CNT/Fe-Ni@RuO_2@PANI-350 demonstrates significant advantages in suppressing the leaching of Ru species. Consequently, the CNT/Fe-Ni@RuO_2@PANI-350 catalyst demonstrates outstanding catalytic activity and stability during the OER process. Notably, Vo in RuO_2 could still be identified in the Ru 3p and O 1s spectra [Supplementary Figure 13] of CNT/Fe-Ni@RuO_2@PANI-350. Spectral deconvolution reveals that the concentration of V_O in RuO_2 remains relatively stable during OER testing. The XRD pattern of CNT/Fe-Ni@RuO_2@PANI-350 after OER operation [Supplementary Figure 14] displays features comparable to those of the initial state. These observations strongly indicate the exceptional structural stability of CNT/Fe-Ni@RuO_2@PANI-350 in water electrolysis.

DFT simulation is further used to reveal the origin of catalytic activity and stability of the CNT/Fe-Ni@RuO_2@PANI-350 catalyst. Specifically, to simulate the CNT/Fe-Ni@RuO_2@PANI-350 composite structure, a Fe-Ni co-doped graphene supported RuO_2 (110) model (denoted as GPE/Fe-Ni@RuO_2) was constructed [Figure 4A]. In the computational model of GPE/Fe-Ni@RuO_2, Fe and Ni atoms are positioned adjacent to each other, representing the Fe-Ni alloy configuration. DFT calculations shown in Figure 4A reveal that the optimized Fe-O bond lengths at the interface of RuO_2 clusters combined with GPE/Fe-Ni and GPE/Fe are 1.737 and 1.740 Å, respectively, which are significantly shorter than those in FeO (2.166 Å) and Fe_2O_3 (1.983 Å). This finding suggests the formation of Fe-O chemical bonds at the interface between RuO_2 clusters and GPE/Fe-Ni or GPE/Fe. The RuO_2 (110) surface was selected because it is the most stable crystal plane of RuO_2[45,46]. In this structural model, graphene (GPE) is used to simulate the carbon material. Calculation results show that the most stable adsorption configuration for RuO_2 loading is achieved in the GPE/Fe-Ni@RuO_2 model, with an adsorption energy of -5.57 eV. The adsorption energies for RuO_2 loading on GPE/Fe and GPE are -5.33 and -3.13 eV, respectively. This configuration of GPE/Fe-Ni@RuO_2 exhibits

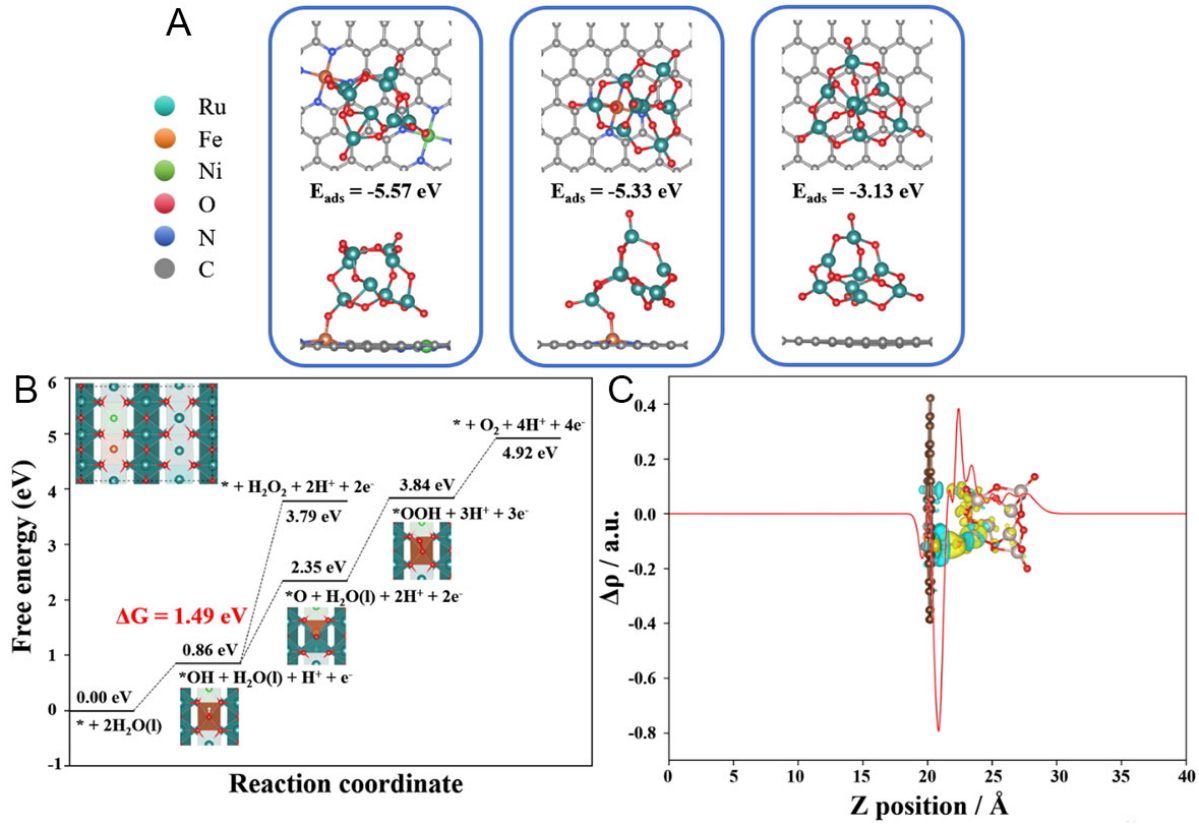

Figure 4. DFT simulations. (A) Optimized geometry of GPE/Fe-Ni@RuO_2, GPE/Fe@RuO_2, and GPE@RuO_2; (B) OER free energy diagram, (C) charge density difference analysis of GPE/Fe-Ni@RuO_2.

Fe-O and Ni-O interactions, confirming that the anchoring-confinement effect of Fe-Ni sites on the graphite surface significantly enhances the preferential loading of RuO_2. Notably, the RuO_2 (110) surface is exposed with a protonated oxygen-terminated form, which closely matches the distinct -OH characteristic peak observed in the O 1s spectrum of CNT/Fe-Ni@RuO_2@PANI-350. From a perspective view of thermodynamics, the more negative adsorption energy between GPE/Fe-Ni and RuO_2 demonstrates a stronger interaction, leading to the formation of a more stable structure. Furthermore, the calculations indicate that the OER active sites are the exposed Ru atomic sites on the RuO_2 (110) surface [Figure 4B]. The corresponding OER free energy diagrams reveal that for the GPE/Fe-Ni@RuO_2 system, both the *OH→*O and *O→*OOH conversions act as rate-determining steps, each exhibiting an energy barrier of 1.49 eV. In contrast, the rate-determining step shifts to the *OOH deprotonation process for both GPE/Fe@RuO_2 and GPE@RuO_2, with a higher energy barrier of 1.80 and 2.22 eV [Supplementary Figure 15], respectively. These theoretical calculations align well with the experimental results, elucidating the underlying mechanism responsible for the enhanced OER catalytic activity of CNT/Fe-Ni@RuO_2@PANI-350.

Charge density analysis was employed to reveal the influence of the catalyst's electronic structure on its OER activity[47]. Figure 4C and Supplementary Figure 16 display the planar average charge density distribution curves of different catalyst models (GPE/Fe-Ni@RuO_2, GPE/Fe@RuO_2, and GPE@RuO_2). Significant charge redistribution is observed at the interface between RuO_2 (110) and graphite substrate under the synergistic effect of Fe-Ni bimetals [Figure 4C]. The yellow regions represent electron density depletion ($\Delta\rho < 0$), while cyan regions indicate electron density accumulation ($\Delta\rho > 0$). Local charge

integration analysis shows that the presence of Fe-Ni bimetals promotes directional charge transfer from RuO_2 to graphite substrate, resulting in a higher oxidation state of Ru sites. The results indicate that the distinct electronic interaction between RuO_2 and graphite substrate with the synergistic effect of Fe-Ni bimetals effectively enhances the oxidation capacity of RuO_2, thereby improving its OER catalytic performance[48]. In contrast, the GPE@RuO_2 model exhibits minimal charge exchange between graphite substrate and RuO_2 clusters in absence of Fe-Ni or Fe. Such a difference in electronic interaction between RuO_2 and graphite substrate is closely related to the anchoring effect of Fe-Ni or Fe sites. Particularly, the planar average charge density curve of GPE/Fe-Ni@RuO_2 shows a sharper peak at the adsorption site for RuO_2, corresponding to the dual-site adsorption configuration induced by the Fe-Ni bimetallic sites. These findings at the electronic level corroborate the intrinsic mechanism that the anchoring-confinement effect of Fe-Ni bimetals on the CNT surface induces the preferential loading of RuO_2 and enhances its catalytic performance.

CONCLUSIONS

In conclusion, the RuO_2 nanoparticles decorated on Fe-Ni-doped CNTs have been prepared as a catalyst for OER in acidic conditions with high catalytic activity and stability. Experimental and theoretical investigations reveal that the nano-confinement effect induced by Fe-Ni bimetals on the CNT surface not only strengthens the anchoring stability of RuO_2 nanoparticles, but also promotes a significant increase in the oxidation state of active-site through interfacial electron coupling. These effects boost the catalytic activity of Ru sites and enhance the surface stability of Ru during OER. As a result, the catalyst exhibits a decent OER performance with overpotential of 188 and 225 mV at a current density of 10 and 100 mA cm^{-2}, respectively, in 0.5 M H_2SO_4. Notably, the catalyst sustains merely 30 mV overpotential increase throughout 150 h continuous operation at 10 mA cm^{-2}. This study proposes a bimetallic nano-confinement strategy addressing the stability of Ru-based catalysts, potentially opening an alternative way for designing OER electrocatalysts with both high activity and long-term stability.

DECLARATIONS

Authors' contributions

Conceptualization and supervision, review and editing: Zhao, Y.; Li, B.
Experimentation: Liu, S.; Tan, H.; Dai, G.
Investigation, methodology: Xiong, S.; Zhao, Y.; Li, B.
Materials characterization: Liu, S.; Dai, G.
Data analysis: Liu, S.; Tan, H.; Xiong, S.
Writing-original draft: Liu, S.

Availability of data and materials

All detailed materials and methods supporting the results of this study are included in the article/ Supplementary Materials. Further inquiries can be directed to the corresponding author(s).

Financial support and sponsorship

This work was supported by National Natural Science Foundation of China (No. 22179031).

Conflicts of interest

All authors declared that there are no conflicts of interest.

Ethical approval and consent to participate

Not applicable.

Consent for publication

Not applicable.

Copyright

REFERENCES

1. Gautam, J.; Lee, S.; Park, S. Strategic structural design of transition metal electrocatalysts for efficient water splitting: a comprehensive review. *Nano. Today.* **2024**, *59*, 102487. DOI
2. Miao, H.; Zhang, D.; Shi, Y.; et al. Ultrasmall noble metal doped Ru_2P@Ru/CNT as high-performance hydrogen evolution catalysts. *ACS. Sustain. Chem. Eng.* **2021**, *9*, 15063-71. DOI
3. Frydendal, R.; Paoli, E. A.; Knudsen, B. P.; et al. Benchmarking the stability of oxygen evolution reaction catalysts: the importance of monitoring mass losses. *ChemElectroChem* **2014**, *1*, 2075-81. DOI
4. Zhu, Y.; Wang, J.; Weiser, G.; et al. Ru single atoms and sulfur anions dual-doped NiFe layered double hydroxides for high-current-density alkaline oxygen evolution reaction. *Adv. Energy. Mater.* **2025**, *15*, 2500554. DOI
5. Wei, J.; Tang, H.; Sheng, L.; et al. Site-specific metal-support interaction to switch the activity of Ir single atoms for oxygen evolution reaction. *Nat. Commun.* **2024**, *15*, 559. DOI PubMed PMC
6. Kim, J. S.; Kim, B.; Kim, H.; Kang, K. Recent progress on multimetal oxide catalysts for the oxygen evolution reaction. *Adv. Energy. Mater.* **2018**, *8*, 1702774. DOI
7. Qin, Y.; Yu, T.; Deng, S.; et al. RuO_2 electronic structure and lattice strain dual engineering for enhanced acidic oxygen evolution reaction performance. *Nat. Commun.* **2022**, *13*, 3784. DOI PubMed PMC
8. Hao, S.; Liu, M.; Pan, J.; et al. Dopants fixation of Ruthenium for boosting acidic oxygen evolution stability and activity. *Nat. Commun.* **2020**, *11*, 5368. DOI PubMed PMC
9. Zhang, L.; Jang, H.; Liu, H.; et al. Sodium-decorated amorphous/crystalline RuO_2 with rich oxygen vacancies: a robust pH-universal oxygen evolution electrocatalyst. *Angew. Chem. Int. Ed.* **2021**, *60*, 18821-9. DOI
10. Yao, Q.; Huang, B.; Zhang, N.; Sun, M.; Shao, Q.; Huang, X. Channel-rich RuCu nanosheets for pH-universal overall water splitting electrocatalysis. *Angew. Chem. Int. Ed.* **2019**, *58*, 13983-8. DOI
11. Lin, C.; Li, J.; Li, X.; et al. In-situ reconstructed Ru atom array on α-MnO_2 with enhanced performance for acidic water oxidation. *Nat. Catal.* **2021**, *4*, 1012-23. DOI
12. Shi, Z.; Li, J.; Wang, Y.; et al. Customized reaction route for ruthenium oxide towards stabilized water oxidation in high-performance PEM electrolyzers. *Nat. Commun.* **2023**, *14*, 843. DOI PubMed PMC
13. Al, Z. W.; Al, M. A.; Hazmatulhaq, F.; et al. Origin of the synergistic effects of bimetallic nanoparticles coupled with a metal oxide heterostructure for accelerating catalytic performance. *SusMat* **2024**, *4*, e216. DOI
14. Zoubi W, Sheng Y, Hussain I, Seongjun H, Thalji MR, Park N. Synthesis and machine learning prediction of high entropy multi-principal element nanoparticles. *Small* **2025**, *21*, e2501444. DOI PubMed
15. Wu, Z. Y.; Chen, F. Y.; Li, B.; et al. Non-iridium-based electrocatalyst for durable acidic oxygen evolution reaction in proton exchange membrane water electrolysis. *Nat. Mater.* **2023**, *22*, 100-8. DOI
16. Zheng, X.; Yang, J.; Xu, Z.; et al. Ru-Co pair sites catalyst boosts the energetics for the oxygen evolution reaction. *Angew. Chem. Int. Ed.* **2022**, *61*, e202205946. DOI
17. Liu, L.; Ji, Y.; You, W.; et al. Trace lattice S inserted RuO_2 flexible nanosheets for efficient and long-term acidic oxygen evolution catalysis. *Small* **2023**, *19*, e2208202. DOI
18. Liu, H.; Zhang, Z.; Fang, J.; et al. Eliminating over-oxidation of ruthenium oxides by niobium for highly stable electrocatalytic oxygen evolution in acidic media. *Joule* **2023**, *7*, 558-73. DOI
19. Zhang, C.; Wang, J.; Ma, H.; et al. Electronic structure engineering of NiFe hydroxide nanosheets via ion doping for efficient OER electrocatalysis. *Chem. Eng. J.* **2024**, *499*, 156430. DOI
20. Zheng, S.; Xu, H.; Zhu, H.; et al. Heterostructured electrocatalysts for the oxygen evolution reaction. *J. Mater. Chem. A.* **2024**, *12*, 18832-65. DOI
21. Wang, H.; Fan, W.; Yang, S.; et al. Deeply understanding electrocatalytic oxygen evolution reaction from the perspective of defect structures. *Chem. Eng. J.* **2024**, *499*, 156124. DOI
22. Zhang, J.; Chen, Q.; Zhao, P.; et al. Room temperature synthesis of gradient-distributed Ni/Fe sites in layered double hydroxides for enhanced oxygen evolution reaction. *Small* **2025**, *21*, e2409265. DOI
23. Mu, X.; Yu, M.; Liu, X.; et al. High-entropy ultrathin amorphous metal-organic framework-stabilized Ru(Mo) dual-atom sites for water oxidation. *ACS. Energy. Lett.* **2024**, *9*, 5763-70. DOI
24. González-ingelmo, M.; García, M. L.; Oropeza, F. E.; et al. Ultra-high dispersion of Ni-based OER catalysts on graphene 3D networks enhances the *in situ* Fe^{3+} catalytic activation. *J. Mater. Chem. A.* **2023**, *11*, 24248-60. DOI
25. Zuo, S.; Wu, Z. P.; Zhang, G.; et al. Correlating structural disorder in metal (Oxy)hydroxides and catalytic activity in electrocatalytic oxygen evolution. *Angew. Chem. Int. Ed.* **2024**, *63*, e202316762. DOI

26. Gao, T.; Kumar, K. S.; Yan, Z.; et al. Covalent organic framework derived synthesis of Ru embedded in carbon nitride for hydrogen and oxygen evolution reactions. *J. Mater. Chem. A.* **2023**, *11*, 19338-48. DOI
27. Wang, Y.; Zhao, L.; Ma, J.; Zhang, J. Confined interface transformation of metal-organic frameworks for highly efficient oxygen evolution reactions. *Energy. Environ. Sci.* **2022**, *15*, 3830-41. DOI
28. Zhang, D.; Miao, H.; Wu, X.; et al. Scalable synthesis of ultra-small Ru_2P@Ru/CNT for efficient seawater splitting. *Chin. J. Catal.* **2022**, *43*, 1148-55. DOI
29. Kresse, G.; Furthmüller, J. Efficiency of ab-initio total energy calculations for metals and semiconductors using a plane-wave basis set. *Comput. Mater. Sci.* **1996**, *6*, 15-50. DOI
30. Kresse, G.; Furthmüller, J. Efficient iterative schemes for ab initio total-energy calculations using a plane-wave basis set. *Phys. Rev. B. Condens. Matter.* **1996**, *54*, 11169-86. DOI PubMed
31. Kresse, G.; Hafner, J. Ab initio molecular-dynamics simulation of the liquid-metal-amorphous-semiconductor transition in germanium. *Phys. Rev. B. Condens. Matter.* **1994**, *49*, 14251-69. DOI PubMed
32. Torres, E.; Kaloni, T. Projector augmented-wave pseudopotentials for uranium-based compounds. *Comput. Mater. Sci.* **2020**, *171*, 109237. DOI
33. Perdew, J. P.; Burke, K.; Ernzerhof, M. Generalized gradient approximation made simple. *Phys. Rev. Lett.* **1996**, *77*, 3865-8. DOI PubMed
34. Grimme, S.; Antony, J.; Ehrlich, S.; Krieg, H. A consistent and accurate ab initio parametrization of density functional dispersion correction (DFT-D) for the 94 elements H-Pu. *J. Chem. Phys.* **2010**, *132*, 154104. DOI PubMed
35. Nørskov, J. K.; Rossmeisl, J.; Logadottir, A.; et al. Origin of the overpotential for oxygen reduction at a fuel-cell cathode. *J. Phys. Chem. B.* **2004**, *108*, 17886-92. DOI
36. Wang, V.; Xu, N.; Liu, J.; Tang, G.; Geng, W. VASPKIT: a user-friendly interface facilitating high-throughput computing and analysis using VASP code. *Comput. Phys. Commun.* **2021**, *267*, 108033. DOI
37. Jin, H.; Li, Z.; Wang, L.; Zeng, Q. Fabrication and properties of CNT /Ni/Y/ZrB_2 nanocomposites reinforced in situ. *J. Am. Ceram. Soc.* **2018**, *101*, 1747-53. DOI
38. Yan, H.; Jiang, Z.; Deng, B.; Wang, Y.; Jiang, Z. Ultrathin carbon coating and defect engineering promote RuO_2 as an efficient catalyst for acidic oxygen evolution reaction with super-high durability. *Adv. Energy. Mater.* **2023**, *13*, 2300152. DOI
39. Xu, Z.; Wang, S.; Tu, W.; et al. A superior bifunctional electrocatalyst in which directional electron transfer occurs between a Co/Ni alloy and Fe-N-C support. *Small* **2024**, *20*, e2401730. DOI
40. Das, D.; Santra, S.; Nanda, K. K. In Situ fabrication of a nickel/molybdenum carbide-anchored n-doped graphene/CNT hybrid: an efficient (Pre)catalyst for OER and HER. *ACS. Appl. Mater. Interfaces.* **2018**, *10*, 35025-38. DOI PubMed
41. Wang, H.; Luan, X.; Li, H.; et al. Ru-M (Fe, Co, Ni) onto nitrogen-doped two-dimensional carbon nanosheets through microwave approach with strong metal-support interactions for overall water-splitting. *Chem. Eng. J.* **2024**, *502*, 158063. DOI
42. Gao, T.; Zhou, C.; Chen, X.; Huang, Z.; Yuan, H.; Xiao, D. Surface *in situ* self-reconstructing hierarchical structures derived from ferrous carbonate as efficient bifunctional iron-based catalysts for oxygen and hydrogen evolution reactions. *J. Mater. Chem. A.* **2020**, *8*, 18367-75. DOI
43. Liu, C.; Sheng, B.; Zhou, Q.; et al. Motivating Ru-bri site of RuO_2 by boron doping toward high performance acidic and neutral oxygen evolution. *Nano. Res.* **2022**, *15*, 7008-15. DOI
44. Jin, H.; Choi, S.; Bang, G. J.; et al. Safeguarding the RuO_2 phase against lattice oxygen oxidation during acidic water electrooxidation. *Energy. Environ. Sci.* **2022**, *15*, 1119-30. DOI
45. Zagalskaya, A.; Alexandrov, V. Role of defects in the interplay between adsorbate evolving and lattice oxygen mechanisms of the oxygen evolution reaction in RuO_2 and IrO_2. *ACS. Catal.* **2020**, *10*, 3650-7. DOI
46. Fang, Y. H.; Liu, Z. P. Mechanism and Tafel lines of electro-oxidation of water to oxygen on RuO_2(110). *J. Am. Chem. Soc.* **2010**, *132*, 18214-22. DOI PubMed
47. Lu, T.; Chen, F. Multiwfn: a multifunctional wavefunction analyzer. *J. Comput. Chem.* **2012**, *33*, 580-92. DOI
48. Ge, R.; Li, L.; Su, J.; Lin, Y.; Tian, Z.; Chen, L. Ultrafine defective RuO_2 electrocatayst integrated on carbon cloth for robust water oxidation in acidic media. *Adv. Energy. Mater.* **2019**, *9*, 1901313. DOI